

Lymph Node Gross Tumor Volume Detection in Oncology Imaging via Relationship Learning Using Graph Neural Network

Chun-Hung Chao¹, Zhuotun Zhu^{†2,3}, Dazhou Guo^{†2}, Ke Yan^{†2}, Tsung-Ying Ho⁴, Jinzheng Cai², Adam P. Harrison², Xianghua Ye⁵, Jing Xiao⁶, Alan Yuille³, Min Sun¹, Le Lu², and Dakai Jin²

¹National Tsing Hua University, Hsinchu City, Taiwan, ROC

²PAII Inc., Bethesda, MD, USA

³ Johns Hopkins University, Baltimore, MD, USA

⁴Chang Gung Memorial Hospital, Linkou, Taiwan, ROC

⁵The First Affiliated Hospital Zhejiang University, Hangzhou, China

⁶Ping An Technology, Shenzhen, China

Abstract. Determining the spread of lymph node gross tumor volume (GTV_{LN}) is essential in defining the respective resection or irradiating regions for the downstream workflows of surgical resection and radiotherapy for many cancers. Different from the more common enlarged lymph node (LN), GTV_{LN} also includes smaller ones if associated with high positron emission tomography signals and/or any metastasis signs in CT. This is a daunting task. In this work, we propose a unified LN appearance and inter-LN relationship learning framework to detect the true GTV_{LN} . This is motivated by the prior clinical knowledge that LNs form a connected lymphatic system, and the spread of cancer cells among LNs often follows certain pathways. Specifically, we first utilize a 3D convolutional neural network with ROI-pooling to extract the GTV_{LN} 's instance-wise appearance features. Next, we introduce a graph neural network to further model the inter-LN relationships where the global LN-tumor spatial priors are included in the learning process. This leads to an end-to-end trainable network to detect by classifying GTV_{LN} . We operate our model on a set of GTV_{LN} candidates generated by a preliminary 1st-stage method, which has a sensitivity of $> 85\%$ at the cost of high false positive (FP) (> 15 FPs per patient). We validate our approach on a radiotherapy dataset with 142 paired PET/RTCT scans containing the chest and upper abdominal body parts. The proposed method significantly improves over the state-of-the-art (SOTA) LN classification method by 5.5% and 13.1% in F1 score and the averaged sensitivity value at 2, 3, 4, 6 FPs per patient, respectively.

Keywords: lymph node gross tumor volume, relationship learning, graph neural network, oncology imaging, radiotherapy

[†] equal contribution.

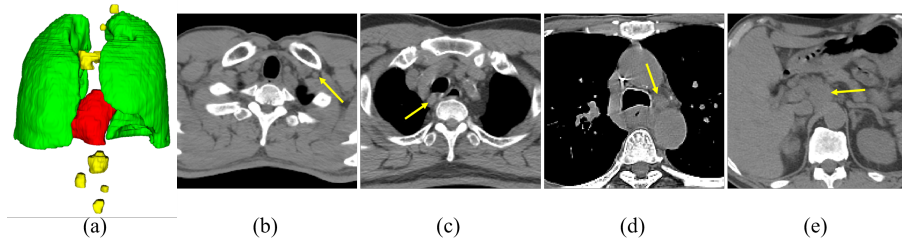


Fig. 1: (a) A 3D rendering of an esophageal tumor (red), lung (green) and the LNs identified by the oncologist (yellow). (b-e) The axial view of the GTV_{LN} spanning from the lower neck to the upper abdomen region. Note that the GTV_{LN} includes the enlarged LN, as well as smaller but suspected metastasized ones.

1 Introduction

Quantitative lymph node (LN) analysis is an important clinical task for cancer staging and identifying the proper treatment areas in radiotherapy. The revised RECIST guideline [4] recommends measuring enlarged LNs (if short axis > 10 mm) for the purpose of tumor burden assessment. However, in cancer treatment, like radiotherapy or surgery, besides the primary tumor, all metastasis-suspected LNs are also required to be treated. This includes the enlarged LNs, as well as other smaller ones that are associated with high positron emission tomography (PET) signals and/or other metastasis signs in CT. This broader category is referred as lymph node gross tumor volume (GTV_{LN}) in radiotherapy treatment. Accurate identification of GTV_{LN} is essential for the delineation of clinical target volume in radiotherapy [11], where missing small but involved GTV_{LN} , will lead to undesired under-treatment [16].

Identifying GTV_{LN} could be a very difficult and time-consuming task, even for experienced radiation oncologists. It requires a sophisticated subjective reasoning process that leads to high inter-observer variabilities [8]. Beside the difficulties already met by detecting enlarged LNs, LNs can exhibit low contrast with surrounding tissues and can be easily confused with other vessel or muscle structures. GTV_{LN} detection has its unique challenges: (1) GTV_{LN} discovery is often performed using radiotherapy CT (RTCT), which, unlike diagnostic CT, is not contrast-enhanced. (2) The size and shape of GTV_{LN} vary considerably, and their locations have an implicit relation with the primary tumor [1]. See Fig. 1 for an illustration of GTV_{LN} . While many previous work developed automatic detection/identification methods for enlarged LNs using contrast-enhanced CT [2, 3, 5, 17, 22], not much work has attempted on the GTV_{LN} identification task. These previous work all focus on characterizing instance-wise LN features. Note that, similar to [17–19], our task assumes there is a set of GTV_{LN} candidates computed from an existing detection system with high sensitivities, but low precision so that we target on effectively reducing the false positive (FP) GTV_{LN} . As shown in our experiments, applying the previous state-of-the-art LN identification by classification method [17] leads to a markedly inferior performance.

Unlike prior work that only assess or identify individual LN separately and independently, we perform a study-wise analysis that incorporates the inter-LN and LN-primary tumor relationships. This is motivated by the fact that our lymphatic system is a connected network of LNs, and tumorous cells often follow certain pathways to spread between the LNs [1]. To achieve this, we propose to use graph neural networks (GNNs) to model this inter-LNs relationship. Specifically, we first train a 3D convolutional neural network (CNN) to extract GTV_{LN} instance-wise appearance features from CT. Then, we compute the 3D distances and angles for each GTV_{LN} with respect to the primary tumor, which serves as the spatial prior of each GTV_{LN} instance. Using the instance-wise appearance features and spatial priors to create node representations, a GNN is built, where relationships between GTV_{LN} are patient adaptive via a learnable features fusion function. This allows the GNN to automatically learn the GTV_{LN} -candidate connection strengths to help distinguishing between true and false GTV_{LN} . The whole CNN and GNN framework is end-to-end trainable, allowing GNN to guide the appearance feature extraction in the CNN. Moreover, PET imaging is included as an additional input channel to the CNN model to provide CT imaging with complementary oncology information, which is demonstratively helpful for GTV_{LN} identification task [8]. We evaluate on a dataset of 142 esophageal cancer patients, as the largest dataset to date. The proposed method significantly improves over the state-of-the-art (SOTA) LN detection/classification method [17, 18] by 5.5% and 13.1% in F1 scores and the averaged sensitivity at 2, 3, 4, 6 FPs per patient, respectively.

2 Methods

Our GTV_{LN} approach combines 3D CNN and GNN networks. Fig. 2 depicts an overview of our method, which consists of three modularized components: (1) a 3D CNN classifier to extract per GTV_{LN} candidate instance-wise visual features; (2) spatial prior computation, including the LN-to-tumor distance and angle calculations; (3) a GNN that learns the inter-LN candidate relationship using the global GTV_{LN} spatial priors and their instance-wise CNN features.

2.1 3D CNN-based Appearance Learning

We first train a CNN to extract the GTV_{LN} instance-wise visual features from CT and PET imaging. We adopt a multi-scale 3D CNN model with a ROI-GAP layer [7] that accepts paired CT/PET image patches. The features generated by each convolutional block separately pass through a 3D ROI-GAP layer and a fully connected layer to form a 256-dimensional vector, which are then concatenated together to generate a multi-scale local representation for each GTV_{LN} candidate. Since we use four CNN blocks, this leads to a $4 \times 256 = 1024$ -dimensional feature vector, which is denoted as f .

2.2 Spatial Prior Computation

In addition to the appearance features, spatial priors can provide crucial information for generating the GNN node representation. We compute each normalized

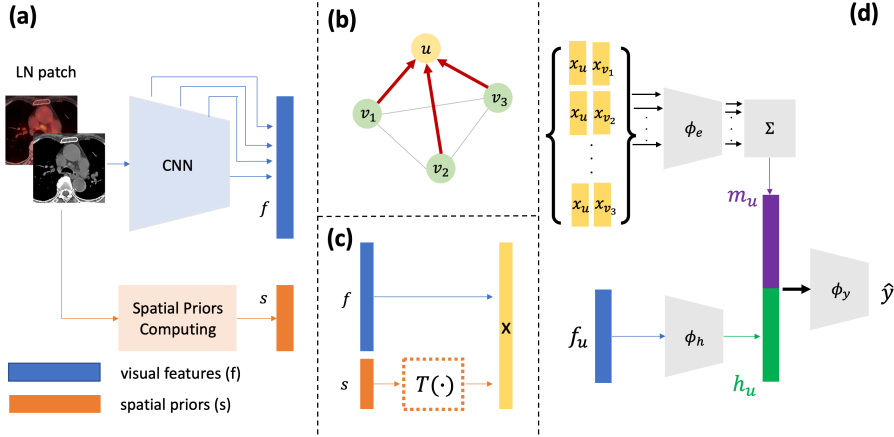


Fig. 2: **System overview.** (a) For each GTV_{LN} candidate, the model extracts CNN appearance features, f , and the spatial priors, s , for each candidate to create node representations, x . (b) We treat each GTV_{LN} candidate as a node in the graph and use proposed GNN to exchange information. Here we take node u as an example for a target node and the red arrow denotes message passing from other nodes. (c) and (d) show how we obtain the node representations and node latent features h , respectively. (d) also depicts how the aggregated passed message, m , and latent features are used to identify GTV_{LN}.

3D spatial coordinates and also 3D distance and angles to the primary tumor. First, to calculate the normalized 3D spatial coordinates we use each patient’s lung mask range in the x and y axes to normalize the GTV_{LN} candidates’ x and y locations. Specifically, we adopt and reimplement a pretrained a 2D progressive holistically nested network (PHNN) [9] to segment the lung, which can perform robustly on pathological lungs. Then we calculate the minimum and maximum coordinates of the lung mask and use these as cutoffs to normalize all candidate x and y location to the range of $[0, 1]$. For the z dimension, we train a fully unsupervised body-part regressor [21] using our dataset to provide the normalized z location for each GTV_{LN} candidate instance.

To compute the distance and angles from any candidate to the primary tumor, we first compute the 3D distance transform from the tumor segmentation mask \mathcal{O} . Let $\Gamma(\mathcal{O})$ be a function that computes all boundary voxels of the tumor mask. The distance transform map (DM) value at a voxel p with respect to \mathcal{O} is computed as

$$\text{DM}_{\Gamma(\mathcal{O}_i)}(p) = \begin{cases} \min_{q \in \Gamma(\mathcal{O}_i)} d(p, q) & \text{if } p \notin \mathcal{O}_i \\ 0 & \text{if } p \in \mathcal{O}_i \end{cases}, \quad (1)$$

where $d(p, q)$ is a distance measure from p to q . We use the Euclidean distance metric and apply Maurer *et al.*’s efficient algorithm [15] to compute the DMs. For calculating the angles of each GTV_{LN} candidate with respect to the tumor, we extract the center point or centerline [12] of the tumor and then calculate the

elevation (θ) and azimuth (ϕ) with respect to the candidate center. We denote all these spatial priors as s .

2.3 GNN-based Iner-LN Relationship Learning

Inter-LN Graph Formulation With the local visual features obtained from the CNN model and the spatial priors calculated in Sec 2.2, we use them to create a node representation, x , for each GTV_{LN} candidate. Because of divergence in construction between the visual features and spatial priors, we use a learnable function, e.g., a multi-layer perceptron (MLP), T to transform the latter to align them better with the CNN visual features:

$$\begin{aligned} s' &= T(s), \\ x &= (f \parallel s'), \end{aligned} \tag{2}$$

where \parallel denotes concatenation. In addition to the node representation, each node has its own latent feature h produced by a learnable function ϕ_h . Since the latent feature is considered a local feature that does not take part in information exchange, we only use the visual features here:

$$h = \phi_h(f). \tag{3}$$

Graph Message Passing Neural Network Message passing neural networks [6] are a widely used basis for GNNs, such as gated graph sequential networks [14], graph attention networks [20], and dynamic graph message passing networks [23]. Given the target node u and its neighboring nodes $\mathcal{N}(u)$, the key idea is to collect information from all of the neighboring nodes, which are usually their node representations and extract the essential information:

$$m_u = \sum_{v \in \mathcal{N}(u)} \alpha_{uv} \cdot \phi_e(x_v), \tag{4}$$

where m_u denotes the message passed to the target node and a function ϕ_e is used to aggregate information from the node neighborhood. Note that all extracted information is weighted by the distance $\alpha \in [0, 1]$ between the neighboring and the target nodes.

The target node u then updates its own latent feature h_u with the message m_u using an updating function ϕ_u :

$$h'_u = \phi_u(h_u, m_u). \tag{5}$$

Common choices for ϕ_u are the linear, gated attention or fully connected layers.

Inter-LN Relationship Modeling The above graph message passing network weights the latent feature vector h by a scalar α , as in (4). However, a more adaptive approach can allow for a more powerful model of the inter-nodal relationship. Hence, we propose to use the representations of both source node

x_v and target node x_u to implicitly model the inter-nodal relationship and generate more informative messages to pass to the target. More formally, we use a learnable function, \mathcal{G} , which can fuse the feature vectors from pairs of nodes:

$$m_u = \sum_{v \in \mathcal{N}(u)} \phi_e(\mathcal{G}(x_u, x_v)). \quad (6)$$

Note that we consider our graph as a fully connected graph with self-connections, thus all the nodes belong to the neighborhood $\mathcal{N}(u)$ of any particular node u . Once all the nodes have their latent features updated, the predictions of each node are made based on their h'_u , which aggregates information all nodes in the graph:

$$\hat{y} = \phi_y(h'_u). \quad (7)$$

3 Experiments and Results

Dataset We collected a dataset of 142 esophageal patients who underwent radiotherapy treatment. In total, there are 651 GTV_{LN} in the mediastinum or upper abdomen region that were identified by an oncologist. Each patient has a non-contrast RTCT scan and a PET scan that has been registered to the RTCT using the method of [10]. We randomly split patients into 60%, 10%, 30% for training, validation and testing, respectively.

GTV_{LN} candidates generation We first use an in-house GTV_{LN} CAD system to generate the GTV_{LN} candidates that will be used in this work [24]. The CAD system achieves 85% sensitivity with a large number of FP detections (> 15 FPs per patient). This leads to > 2000 FPs that serve as negative GTV_{LN} candidates. For the ease of comparison, similar to [17], we also include the ground-truth GTV_{LN} in the set of true GTV_{LN} candidates for training. This ensures 100% sensitivity at the GTV_{LN} candidate generation step.

Image preprocessing and implementation details We resample the RTCT and registered PET images to a consistent spatial resolution of $1.0 \times 1.0 \times 1.0$ mm. The 3D training patch is generated by cropping a $48 \times 48 \times 48$ sub-volume centered around each GTV_{LN} candidate. If the size of the GTV_{LN} is larger than $48 \times 48 \times 48$, we resize the sub-volume so that it contains at least an 8-voxel margin of the background along each dimension to ensure sufficient background context. For the training sample generation for the 2.5D LN classification method [17], we adopt the preprocessing method described in that paper. Our 3D CNN is trained using the Adam [13] optimizer with a learning rate of 0.0001 and batch size of 32 for 10 epochs.

For the GNN part, the parameters of the first layer in the CNN are loaded from the CNN baseline model reported in Table 1. The feature aligning function T for spatial priors can be either a simple repeat function or a MLP. We opt for the latter approach, choosing an output dimension size of 640. We also use MLPs for ϕ_e and ϕ_h which reduce the input dimension from 3328 and 1024, respectively, to 256. The entire GNN architecture is trained with Adam optimizer whose learning rate is set to 0.0001. Since the numbers of GTV_{LN} candidates vary from

patient to patient, the nodes in GNN changed dynamically. To accommodate different graph sizes, we set batch size as 1 and adopted gradient accumulation strategy which is equivalent to using batch size 8 during training.

Comparison setup and evaluation metrics We compare against the SOTA instance-wise LN classification method [17], which uses a random view aggregation in a 2.5D fashion to learn the LN local representations. We also compare against a CNN-based classifier (both 2.5D and our 3D input) under various input settings: CT alone, CT+PET. We also compared against the GNN with the weight in the adjacency matrix (α_{uv} in (4)) regressed by an additional module [20], denoted as **CNN+GNN_b**. Our method is denoted as **CNN+GNN_p**.

To evaluate performance, we compute the free response operating characteristic (FROC), which measures the recall against different numbers of FPs allowed per patient. We also report the average sensitivity (mFROC) at 2, 3, 4, 6 FPs per patient.

Table 1: Quantitative results of our proposed methods with the comparison to other setups and the previous state-of-the-art. Note, we use ResNet18 as the CNN backbone. The GNN_b and GNN_p denote the baseline and proposed GNNs, respectively. S.P. denotes the spatial prior features of GTV_{LN}.

Method	2.5D	3D	CT	PET	S.P.	F1	mFROC
Roth et. al [17]	✓		✓			0.483	0.537
Roth et. al [17]	✓		✓	✓		0.498	0.561
CNN		✓	✓			0.493	0.568
CNN		✓	✓		✓	0.516	0.602
CNN		✓	✓	✓		0.517	0.595
CNN		✓	✓	✓	✓	0.505	0.597
CNN + GNN _b		✓	✓		✓	0.500	0.593
CNN + GNN _b		✓	✓	✓	✓	0.521	0.631
CNN + GNN _p		✓	✓	✓	✓	0.504	0.631
CNN + GNN _p		✓	✓	✓	✓	0.538	0.668

Quantitative Results and Discussions Table 1 outlines the quantitative comparisons of different model setups and choices. First, several conclusions can be drawn to validate the effectiveness of our CNN-based classification method. (1) The SOTA instance-wise 2.5D LN classification method [17] exhibits markedly decreased performance as compared to our 3D CNN in both CT and CT+PET input settings, *e.g.*, [17] has a mFROC of 0.561 with CT+PET inputs as compared to 0.595 achieved by our 3D CNN model with CT+PET inputs. This demonstrates that the direct 3D convolution is at least as effective as the pseudo 3D method [17] for the LN identification problem. (2) PET modality plays an important role in the GTV_{LN} detection, since both 2.5D and 3D CNN gain consistent mFROC improvement after adding PET as an additional input channel. (3) Spatial prior features are useful for the CT based CNN classifier, however, it does not add value when the CNN is already trained with CT+PET. This may be due to the fact that the instance-wise GTV_{LN} features extracted

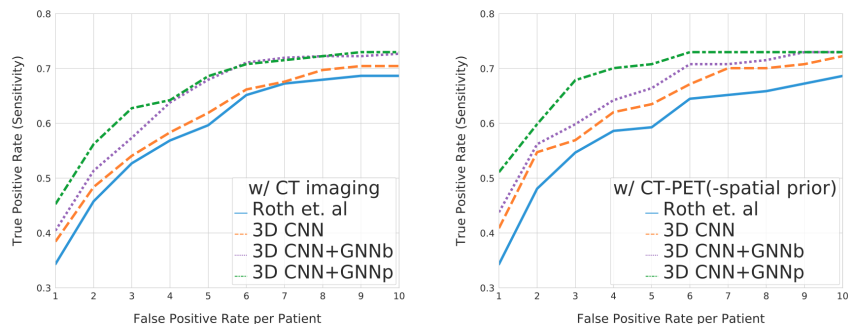


Fig. 3: Free-response receiver operating characteristic (FROC) curves of different GTV_{LN} classification methods under the setting of **CT** (Left) imaging or **CT+PET** (Right) imaging. The proposed method (GNN_p) outperforms the baseline 3D CNN and the node-level feature fusion GNN (GNN_b) by some marked margins under both imaging settings.

from CT+PET reached the saturated classification capacity, however, the spatial priors provide useful information if features are extracted from CT alone.

When further considering the inter-LN relation captured by the GNN model, the GTV_{LN} classification performance is consistently boosted. For example, under the CT+PET input with the spatial prior setting, both the CNN+ GNN_b and CNN+ GNN_p outperform the corresponding 3D CNN model by a large margin, *i.e.*, 3.4% and 6.9% in mFROC metrics, respectively. This validates our observation and intuition that the LNs form a connected network and cancers often follow certain pathways spreading to the LNs. Hence, learning the inter-LN relationship should be beneficial to distinguish the metastasis-suspicious GTV_{LN} . Moreover, our proposed element-level feature fusion method in the GNN achieves the highest classification performance under both CT and CT+PET input settings as compared to a competing node-level feature fusion method [20]. FROC curves are compared in Fig. 3 for the CNN+GNN methods and the 3D CNN method under different imaging settings. It can be seen that at an operating point of 3 FP/patient, our CNN+ GNN_p improve the sensitivity by 7.3% (55.5% to 62.8%) and 11.0% (56.9% to 67.9%) over the 3D CNN model using the CT and CT+PET imaging, respectively. This further demonstrates the value of the inter-LN relationship learning in the GTV_{LN} classification task. Some qualitative examples are illustrated in Fig. 4.

4 Conclusion

In this paper, we propose a joint 3D deep learning framework on modeling both LN appearance and inter-LN relationship for effective identification of GTV_{LN} . The inter-LN relationship is expected to capture the prior spatial structure of the connected lymphatic system where the spread of cancer cells must follow certain pathways. We combine the process of two 3D CNN (appearance encoding)

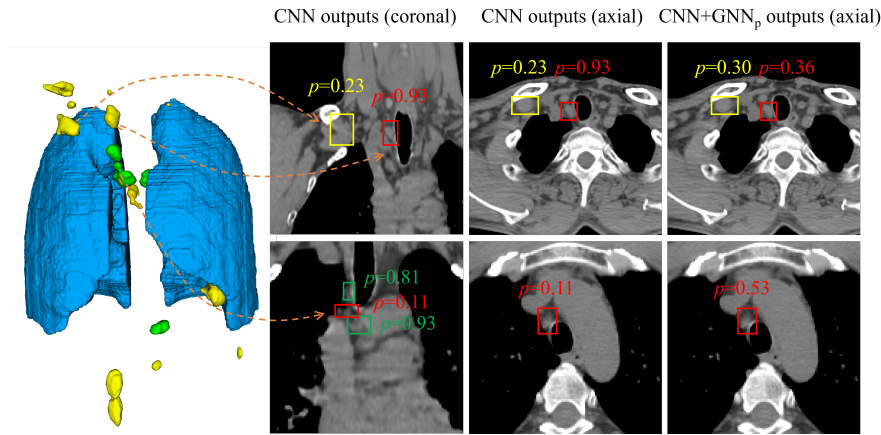


Fig. 4: A quality example illustrating the classification probabilities computed by the 3D CNN based LN instance-wise classifier and by our proposed CNN+GNN_p classifier. Left is the 3D rendering of the GTV_{LN} candidates with yellow as FPs from an in house CAD system [24] and green as the true GTV_{LN}. The top row shows an example where a FP exists at the mediastinum region near the shoulder by the CNN classifier (shown in red with probability of 0.93). Due to the fact that a nearby LN candidate has a low probability of 0.23 (indicate in yellow), and they share a similar location and appearance. This candidate is correctly identified as FP by our CNN+GNN_p classifier. Similar situation is observed for the right bottom row, where a small LN (shown in red) has misclassified by the CNN model, but is able to correctly identified by our model due to the fact that there are two nearby strong true candidates (indicated in green) and their appearance is similar.

and GNN (iner-LN relationship learning) networks, which still leads to an end-to-end trainable network. We perform our unified CNN-GNN identification by classification model on a set of GTV_{LN} candidates that are generated by a preliminary 1st-stage method with very high detection sensitivity, but at a lower precision level. We validate our approach on a esophageal radiotherapy dataset of 142 patients and total 651 GTV_{LN}. Our quantitative performance demonstrates significant improvements over previous state-of-the-art LN classification work.

References

1. Akiyama, H., Tsurumaru, M., Udagawa, H., Kajiyama, Y.: Radical lymph node dissection for cancer of the thoracic esophagus. *Annals of surgery* **220**(3), 364 (1994)
2. Barbu, A., Suehling, M., Xu, X., Liu, D., Zhou, S.K., Comaniciu, D.: Automatic detection and segmentation of lymph nodes from ct data. *IEEE Transactions on Medical Imaging* **31**(2), 240–250 (2011)
3. Bouget, D., Jørgensen, A., Kiss, G., Leira, H.O., Langø, T.: Semantic segmentation and detection of mediastinal lymph nodes and anatomical structures in ct data for lung cancer staging. *International journal of computer assisted radiology and surgery* pp. 1–10 (2019)

4. Eisenhauer, E.A., Therasse, P., Bogaerts, J., Schwartz, L.H., Sargent, D., Ford, R., Dancey, J., Arbuck, S., Gwyther, S., Mooney, M., et al.: New response evaluation criteria in solid tumours: revised recist guideline (version 1.1). *European journal of cancer* **45**(2), 228–247 (2009)
5. Feulner, J., Zhou, S.K., Hammon, M., Hornegger, J., Comaniciu, D.: Lymph node detection and segmentation in chest ct data using discriminative learning and a spatial prior. *Medical image analysis* **17**(2), 254–270 (2013)
6. Gilmer, J., Schoenholz, S.S., Riley, P.F., Vinyals, O., Dahl, G.E.: Neural message passing for quantum chemistry. In: *Proceedings of the 34th International Conference on Machine Learning-Volume 70*. pp. 1263–1272. JMLR. org (2017)
7. Girshick, R.: Fast r-cnn. In: *Proceedings of the IEEE international conference on computer vision*. pp. 1440–1448 (2015)
8. Goel, R., Moore, W., Sumer, B., Khan, S., Sher, D., Subramaniam, R.M.: Clinical practice in pet/ct for the management of head and neck squamous cell cancer. *American Journal of Roentgenology* **209**(2), 289–303 (2017)
9. Harrison, A.P., Xu, Z., George, K., Lu, L., Summers, R.M., Mollura, D.J.: Progressive and multi-path holistically nested neural networks for pathological lung segmentation from ct images. In: *International conference on medical image computing and computer-assisted intervention*. pp. 621–629. Springer (2017)
10. Jin, D., Guo, D., Ho, T.Y., Harrison, A.P., Xiao, J., Tseng, C.k., Lu, L.: Accurate esophageal gross tumor volume segmentation in pet/ct using two-stream chained 3d deep network fusion. In: *International Conference on Medical Image Computing and Computer-Assisted Intervention*. pp. 182–191. Springer (2019)
11. Jin, D., Guo, D., Ho, T.Y., Harrison, A.P., Xiao, J., Tseng, C.k., Lu, L.: Deep esophageal clinical target volume delineation using encoded 3d spatial context of tumors, lymph nodes, and organs at risk. In: *International Conference on Medical Image Computing and Computer-Assisted Intervention*. pp. 603–612. Springer (2019)
12. Jin, D., Iyer, K.S., Chen, C., Hoffman, E.A., Saha, P.K.: A robust and efficient curve skeletonization algorithm for tree-like objects using minimum cost paths. *Pattern recognition letters* **76**, 32–40 (2016)
13. Kingma, D.P., Ba, J.: Adam: A method for stochastic optimization. *arXiv preprint arXiv:1412.6980* (2014)
14. Li, Y., Tarlow, D., Brockschmidt, M., Zemel, R.: Gated graph sequence neural networks. *arXiv preprint arXiv:1511.05493* (2015)
15. Maurer, C.R., Qi, R., Raghavan, V.: A linear time algorithm for computing exact euclidean distance transforms of binary images in arbitrary dimensions. *IEEE Transactions on Pattern Analysis and Machine Intelligence* **25**(2), 265–270 (2003)
16. Network, N.C.C.: Nccn clinical practice guidelines:head and neck cancers. *American Journal of Roentgenology* **version 2** (2020)
17. Roth, H.R., Lu, L., Liu, J., Yao, J., Seff, A., Cherry, K., Kim, L., Summers, R.M.: Improving computer-aided detection using convolutional neural networks and random view aggregation. *IEEE transactions on medical imaging* **35**(5), 1170–1181 (2016)
18. Roth, H.R., Lu, L., Seff, A., Cherry, K.M., Hoffman, J., Wang, S., Liu, J., Turkbey, E., Summers, R.M.: A new 2.5 d representation for lymph node detection using random sets of deep convolutional neural network observations. In: *International conference on medical image computing and computer-assisted intervention*. pp. 520–527. Springer (2014)
19. Seff, A., Lu, L., Barbu, A., Roth, H., Shin, H.C., Summers, R.M.: Leveraging mid-level semantic boundary cues for automated lymph node detection. In: *International Conference on Medical Image Computing and Computer-Assisted Intervention*. pp. 53–61. Springer (2015)

20. Veličković, P., Cucurull, G., Casanova, A., Romero, A., Lio, P., Bengio, Y.: Graph attention networks. ICLR (2018)
21. Yan, K., Lu, L., Summers, R.M.: Unsupervised body part regression via spatially self-ordering convolutional neural networks. In: 2018 IEEE 15th International Symposium on Biomedical Imaging (ISBI 2018). pp. 1022–1025. IEEE (2018)
22. Yan, K., Tang, Y., Peng, Y., Sandfort, V., Bagheri, M., Lu, Z., Summers, R.M.: Mulan: Multitask universal lesion analysis network for joint lesion detection, tagging, and segmentation. In: International Conference on Medical Image Computing and Computer-Assisted Intervention. pp. 194–202. Springer (2019)
23. Zhang, L., Xu, D., Arnab, A., Torr, P.H.: Dynamic graph message passing networks. arXiv preprint arXiv:1908.06955 (2019)
24. Zhu, Z., Yan, K., Jin, D., Cai, J., Ho, T.Y., Harrison, A.P., Guo, D., Chao, C.H., Ye, X., Xiao, J., et al.: Detecting scatteredly-distributed, small, and critically important objects in 3d oncology imaging via decision stratification. arXiv preprint arXiv:2005.13705 (2020)